RSC Advances

ROYAL SOCIETY OF CHEMISTRY

www.rsc.org/advances

RSC Advances

ARTICLE

Facile Formation of Hierarchical TiO_2-SnO_2 Nanocomposite Architecture for Efficient Dye-Sensitized Solar Cells

Received 00th January 20xx,
Accepted 00th January 20xx

DOI: 10.1039/x0xx00000x

www.rsc.org/

C. K. Lim,[a,b] † Y. Wang[a] and L. Zhang[b]

In this paper, the hierarchical nanocomposite architecture consists of TiO_2 nanoflakes on SnO_2 nanofiber was successfully synthesized using a simple and cost-effective hydrothermal method. The correlation between the structural changes in nanoflakes sizes and density in accordance with the prolongation of hydrothermal growth duration was observed and discussed using high resolution scanning and transmission electron microscopes. The dye-sensitized solar cells (DSSCs) utilizing these double-layered TiO_2-SnO_2 hierarchical nanostructures as photoelectrode exhibited significant improvement in the photovoltaic properties. In particular, the DSSC made from 24 hrs hydrothermally grown TiO_2 nanoflakes on the surface of SnO_2 nanofibers stood out to be the best performing cells, delivered a promising efficiency of 3.73 %, which was more than 4-fold increment over the DSSC with SnO_2 nanofibers alone. This enhancement was attributed to the superiority in dye-loading and light scattering properties of hierarchical architecture. Benefiting from the constituent advantages of both materials, the photoelectrode with hierarchical nanostructures also inhibited back electron transfer to reduce the electron recombination, leading to improved electron lifetime. These results suggest that simple strategy to synthesize hierarchical nanostructures for efficient DSSC was achieved.

1. Introduction

Since the introduction of low cost, high efficiency dye-sensitized solar cells (DSSCs) in 1991 by O'Regan and Grätzel, it has emerged as a potential alternative to conventional thin film solar cells.[1] A typical DSSC consists of a few micrometer-thick nanocrystalline oxide covered with a monolayer of Ru-dye, a redox electrolyte and a platinum counter electrode. So far, the conventional DSSCs using ruthenium- and porphyrin-based sensitizer have achieved respectable efficiencies of ~11.0 % and 13.0 % respectively.[2-4] Recent breakthrough in the development of DSSC has been demonstrated using organic halide perovskite (e.g. $CH_3NH_3PbX_3$, X =Br, I, Cl or their combinations) as photosensitizer whereby the power conversion efficiency of over 15.0 % was achieved.[5] Over the past two decades, significant research efforts have been devoted on the various components of DSSC to further improve the energy conversion efficiency. While metal complexes and organic dyes are widely developed, natural and vegetable dyes as sensitizer for DSSC are also gaining more attentions due to their "environmental friendly" characteristics while producing promising photovoltaic efficiency ~ 2.7%.[6-8] Extensive research activities have been carried out as well to replace the liquid electrolytes in DSSC into solid-state or quasi solid-state electrolytes in order to enhance the stability and efficiency of DSSC.[9-11] New counter electrode materials utilizing carbon-based nanomaterials have also been investigated and applied in DSSC as alternative to Pt-coated FTO glasses to improve the charge transfer properties.[4,12,13] The choice and the architecture of wide band gap oxide semiconductor is also an interesting research topic that has been extensively studied to improve the conversion efficiency of DSSC.[14,15] The mesoporous semiconductor oxide layer deposited on the transparent conducting oxide (TCO) glass substrate as the photoelectrode, is an essential constituent structure of the DSSC in separating and transferring the photo-generated electrons in the dye sensitizer towards the collection electrode. Currently, TiO_2 is the favored metal oxide for DSSCs. Several alternative oxide semiconductor materials such as ZnO,[16,17] SnO_2,[18,19] $SrTiO_3$,[20] Nb_2O_5[21] and $BaSnO_3$[22] have been investigated for their potential in substituting the TiO_2 as photoelectrode. Among them, SnO_2 stands out to be a potential candidate for DSSCs.

One of the key advantages of SnO_2 over TiO_2 is that SnO_2 offers higher electron mobility (100 to 200 $cm^2\ V^{-1}S^{-1}$) which can be translated into faster transport of photo-injected electrons for

[a] Biomedical Engineering and Materials Group, School of Engineering, 180, Ang Mo Kio Avenue 8, Singapore 569830.
[b] Temasek Laboratories @ Nanyang Technological University, 50 Nanyang Drive, Singapore 637553.
† Corresponding Author: limc0105@e.ntu.edu.sg

Electronic Supplementary Information (ESI) available: [Calculated grain size from XRD pattern; Thermolgravimetric analysis (TGA) of electrospun SnO_2 nanofibers; SEM images of hierarchical TiO_2-SnO_2 nanostructures after annealing; Energy Dispersive X-ray (EDX) measurement of hierarchical TiO_2-SnO_2 nanostructures; Dye absorbance measurements.]. See DOI: 10.1039/x0xx00000x

collection.[23] Other than that, SnO_2 also possesses wider band gap (3.6 eV) than anatase TiO_2 (3.2 eV), which creates less oxidative holes in the valence band under UV illumination to minimize the dye degradation rate and improve the long-term stability of DSSCs.[24] However, the use of SnO_2 is also limited by a few drawbacks. The inferior performance of the DSSCs with SnO_2 photoelectrode has been attributed to higher electron recombination rate due to the 300 mV positive shift of the conduction-band edge of SnO_2 with respect to TiO_2.[25] Other than that, the lower isoelectric point also leads to poorer dye loading.[26] The rate of electron injection from the sensitizer to the conduction band of SnO_2 was also found to be also much slower as compared to TiO_2.[27] As proposed by Goodenough and co-workers, the dehydrative coupling of carboxylic acid groups with surface TiO_2 formed ester-type linkages.[28] The π* orbitals of the dcb ligand would promote rapid excited-state electron injection into the conduction band of TiO_2, which mainly composed of unfilled d orbitals. On the other hand, the SnO_2 possesses predominantly s-orbital character. The Sn s orbitals are orthogonal to the carboxylate π system resulting in less favorable orbital mixing.[29] Hence, the electron injection rates into conduction band of SnO_2 are not as efficient as TiO_2.These issues have been addressed by incorporating a core-shell structure with interfacial layers of wide band gap oxides, such as TiO_2,[30-32] MgO[33,34]or Al_2O_3[35] in between the SnO_2 and dye sensitizer. By using this core-shell system, a better charge separation has been achieved by suppressing charge recombination in the coupled oxide semiconductors system with different energy levels.

The development of one-dimensional (1D) metal-oxide architectures have also been explored for DSSCs to overcome the poor interconnectivity in between the nanoparticles that resulted in high charge recombination losses.[36,37] These ordered nanomaterials have contributed to faster electron transport and slower charge recombination in DSSCs. One simple and versatile technique for producing continuous ultrafine nanofibers in nanometer scale diameter is through electrospinning.[38-40] Electrospinning of 1D polycrystalline SnO_2 nanomaterials with extremely high aspect ratios and specific surface areas have been reported and investigated in many functional applications such as solar cells,[41] photocatalysis,[42,43] batteries[44] and gas sensor.[45,46]

In this work, we propose a simple approach to revamp 1D SnO_2 nanofibers to three-dimensional (3D) hierarchical TiO_2-SnO_2 nano-architecture. This redefined core-shell nanostructure was achieved by hydrothermally growth of TiO_2 nanoflakes for different durations on the SnO_2 nanofibers. Then, the resulting TiO_2-SnO_2 hierarchical heterostructures were characterized and fabricated into the photoelectrode for DSSCs. To study the effects of these double-layered TiO_2-SnO_2 hierarchical heterostructures as photoelectrode, the photovoltaic properties of these DSSCs were investigated in details.

2. Experimental

2.1 Electrospinning of SnO_2 nanofibers

A solvent containing 22 g of ethanol and 22 g of N,N-dimethyl formamide (DMF) were mixed together using magnetic stirring for 1 hr at room temperature. Then, 2.67 g of tin (II) chloride dihydrate ($SnCl_2 \bullet 2H_2O$) was added into the mixed solvent under stirring condition until it was completely dissolved. Subsequently, 4 g of polyvinyl pyrrolidone (PVP, M_w= 1 300 000 g/mol) was added into the resulting solution under vigorous stirring for 2 hrs at room temperature to form a homogenized viscous precursor. The as-prepared precursor solution was then transferred into a plastic syringe for electrospinning. The electrospinning solution was fed at a speed of 1.5 ml/hr. The voltage applied to the tip was 20 kV and the distance between the needle tip and the collector plate was 10 cm. During the electrospinning process, the solution on the tip of the needle was ejected under strong electric field to form a dense fiber membrane on a collector of aluminium foil. Then, the fiber membrane was manually peeled off from the aluminium foil and calcinated at 500 °C for 2 hrs with a heating rate of 1.0 °C/min to remove the PVP content. Finally, the electrospun SnO_2 nanofibers were obtained.

2.2 Preparation of SnO_2 nanofiber photoelectrodes

The electrospun SnO_2 nanofibers were firstly dispersed in ethanol using stirring and ultrasonication to form a homogenized colloidal. Next, this homogenized colloidal was poured into the beaker containing 10 wt% ethyl cellulose (Aldrich) in ethanol prepared earlier. Finally, alpha-terpineol (97%, Aldrich) was added into the colloidal and stirred. The colloidal was then heated up to 80 °C under stirring on a hotplate to evaporate the ethanol content. Finally, a thick homogenized paste was formed and it was deposited on the FTO glass using doctor blade method. The as prepared photoelectrodes made of SnO_2 nanofibers were subjected to annealing at 450°C in air for 30 minutes.

2.3 Synthesis of TiO_2-SnO_2 hierarchical nanostructures

The TiO_2-SnO_2 hierarchical nanostructures were grown using hydrothermal method. First, 0.1 ml of titanium isopropoxide (TTIP, 97%, Aldrich) was added to 50 mL of a 0.45 *M* hydrochloric acid solution under vigorous stirring at room temperature for 2 hrs until a clear solution was obtained. Then, the solution was transferred to a Teflon vessel. The SnO_2 nanofibers and photoelectrodes prepared earlier were immersed into solution in the Teflon vessel. Then, the vessel was placed into the stainless steel autoclave for hydrothermal growth at temperature 95 °C for 3, 7, 15 and 24 hours respectively. After the hydrothermal process, the nanofibers and photoelectrodes were taken out and rinsed thoroughly with DI water. The photoelectrodes with mesoporous TiO_2-SnO_2 hierarchical nanostructures from different growth durations were ready for use.

2.4 Fabrication of DSSC

The photoelectrodes with mesoporous TiO_2-SnO_2 hierarchical nanostructures were soaked in 40 mM $TiCl_4$ (99%, Merck) solution at 70 °C for 30 minutes, followed by annealing at 450 °C for 30 minutes in air. Next, the freshly-annealed photoelectrodes were dipped into the 0.25 mM N719 dye solution (Solaronix) for overnight. The platinum coated counter electrode was then clamped onto the photoelectrode, with the Surlyn spacer (30 µm) in between. Finally, the iodide electrolyte (Solaronix, Iodolyte AN50) was filled through capillary action in vacuum condition to allow the complete infiltration of electrolyte into the mesoporous layer. The DSSCs prepared were ready for photovoltaic testing. A total of five different types of photoelectrodes made from pristine SnO_2 nanofibers (Sample SS) and composites TiO_2-SnO_2 hierarchical nanostructures grown at different hydrothermal durations (3 hrs for sample TS03, 7 hrs for sample TS07 , 15 hrs for sample TS15 and 24 hrs for sample TS24) were prepared for investigation.

2.5 Characterizations

The crystallography of the electrospun SnO_2 fiber and hierarchical nanostructures TiO_2 on SnO_2 nanofibers were studied using X-ray diffraction (XRD) measurements. The XRD patterns were recorded at room temperature using Pan Analytical X'Pert Pro MPD X-ray diffractometer with Cu K-alpha radiation (λ = 1.5406 Å) operating at 40 kV and 40 mA. The surface morphologies of the nanofibers were observed using field emission scanning electron microscope (FESEM, JEOL-JSM-6701F) and Field Emission Transmission Electron Microscopy (TEM, JEOL-JEM 2010F). The PerkinElmer Lambda 950 UV/Vis/NIR spectrophotometer system was used to determine the amount of dye adsorbed onto the photoelectrode. The dye desorption was carried out in a mixed solution of water and ethanol containing 0.1 M NaOH. The current-voltage (*I-V*) curves of the solar cells were measured under simulated solar light irradiation with intensity of 100 mW/cm^2. Electrochemical Impedance measurements were carried out using Metrohm Autolab system in the frequency range of 1 mHz to 1000 kHz at room temperature, illuminated under solar light with intensity of 100 mW/cm^2. The applied bias was set to be the open circuit potential of the DSSC and the ac amplitude was 10 mV.

3. Results and discussion

3.1 Material characterizations

The phase purity and crystal structure of the as-electrospun SnO_2 nanofibers and the hydrothermal growth of TiO_2-SnO_2 hierarchical heterostructures for different durations were determined by XRD, as shown in Fig. 1. After the annealing at 500 °C for 2 hrs, all the peaks in the XRD patterns for SnO_2 nanofibers were indexed accordingly for the cassiterite phase (space group P42/mnm) of SnO_2 (JCPDS file 41-1445). No impurity or secondary phase could be detected in the XRD pattern of SnO_2 nanofibers. The as-synthesized SnO_2 nanofibers were polycrystalline and the crystalline particle size was estimated by using the Scherrer equation, D = 0.9λ/β(cos θ), where λ is the wavelength of the X-ray (1.54 Å), β is the full-width at half-maximum (FWHM) in radians, and θ is the Bragg angle in the diffraction pattern. Using this equation, the mean crystalline particle size was estimated to be 13.9 nm.

Compared with the pristine SnO_2 nanofibers, additional XRD characteristic peaks of rutile TiO_2 could be observed for the case of composite TiO_2-SnO_2 hierarchical heterostructures. The co-existence of the tetragonal SnO_2 and TiO_2 phases has confirmed that the formation of bilayered hierarchical structure with TiO_2 nanocrystallites grown on the surface of SnO_2 nanofibers through the facile single-step hydrothermal process. There was no other diffraction peak indicating the formation of any new composite. With the prolonged growth duration from 3 hrs to 24 hrs, the overall peak intensity of the TiO_2 became more prominent, resulted in the peak intensity of SnO_2 to be partially screened off. This suggests that the presence and growing amount of TiO_2 nanostructures formed on top of the surfaces of SnO_2 nanofibers. Increasing the hydrothermal growth duration has also contributed to larger average sizes of TiO_2 nanocrystallites sizes as calculated based on the Scherrer equation (Supporting information S1).

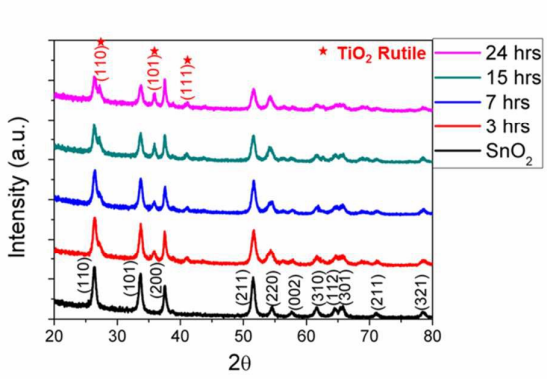

Figure 1. XRD patterns of SnO_2 nanofibers and TiO_2-SnO_2 hierarchical heterostructures hydrothermally grown at different durations (3, 7, 15 and 24 hrs).

The morphologies of the electrospun SnO_2 nanofibers and the corresponding TiO_2-SnO_2 hierarchical heterostructures were investigated by FESEM. Fig. 2a presents the FESEM images of electrospun SnO_2 nanofibers after annealed at 500 °C in air for 2 hrs. The SnO_2 nanofibers were randomly oriented with rough porous structure after the PVP was completely decomposed (Supporting information S2). The size of SnO_2 nanofibers was around 150 - 200 nm in diameter and lengths could reach up to a few tens of micrometers. Observation at higher magnification as shown in Fig. 2a (ii) reveals that the nanofibers were formed by SnO_2 nanoparticles that were densely packed together to create a long and compact fibrous structure. The rough surface of SnO_2 nanofibers is beneficial for high amount of adsorption of dye molecules.

The FESEM images in Fig. 2(b) – (e) reveal that the time dependent study (3, 7, 15, 24 hrs) of hierarchical nano-architecture formed by TiO_2 nanoflakes hydrothermally grown

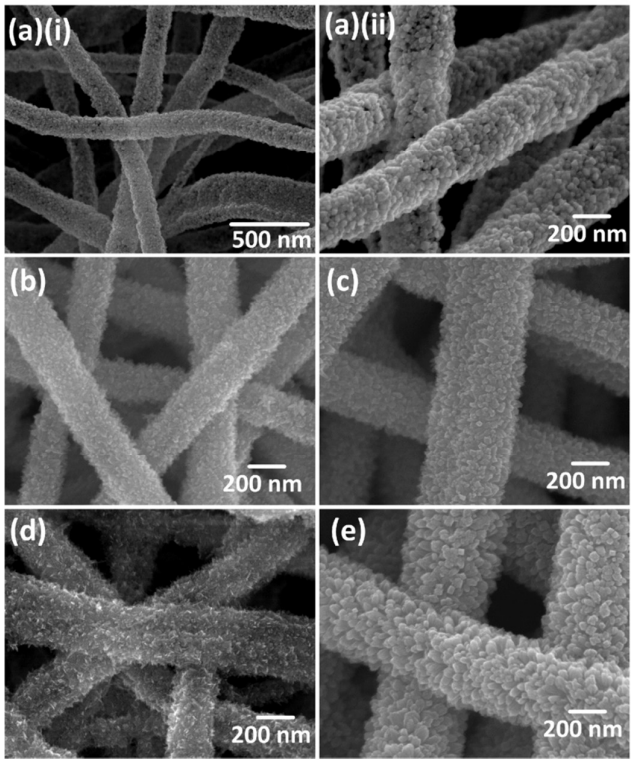

Figure 2. SEM images of TiO_2-SnO_2 hierarchical heterostructures hydrothermally grown at different durations. (a-i/ii) Pristine SnO_2 nanofibers at different magnifications; (b) 3 hrs; (c) 7 hrs; (d) 15 hrs; (e) 24 hrs.

on the SnO_2 nanofibers. The length of these hierarchical nano-architectures maintained at several tens of micrometers (Supporting information S3). This shows that the incorporation of TiO_2 nanoflakes using hydrothermal method did not destroy the tubular nanofibers structure. In this case, the TiO_2 nanoflakes were evenly distributed to form a uniform coating along the length of nanofibers. Hence, the SnO_2 nanofibers can be regarded as the basic matrix for the TiO_2 nanoflakes to grow and form the composite hierarchical nanostructures. In the initial 3 and 7 hrs growth as shown in Fig. 2b and 2c, tiny TiO_2 nanoflakes nucleated on the surfaces of SnO_2 nanofibers. Further prolongation of the hydrothermal growth to 15 hrs (Fig. 2d) resulted in the enhancement of filling rate between the adjacent SnO_2 nanoparticles and the TiO_2 nanoflakes to form a densely populated nanoflakes network. Finally, when the hydrothermal growth duration was extended to 24 hrs, numerous TiO_2 nanoflakes started to evolve into this prominent hierarchical nano-architecture as revealed in Fig. 2e. The average diameter of these nanofibers has also increased noticeably. In short, a hierarchical heterostructures composed of large amount of TiO_2 nanoflakes arrays on SnO_2 nanofibers were successfully achieved using this facile one-step hydrothermal process.

The morphology and crystallinity of SnO_2 nanofibers and TiO_2 nanoflakes were further investigated in details using TEM. Fig 3a depicts a TEM of an individual SnO_2 nanofiber with the tube-shaped structure with hollow core and a wall thickness of about 20 nm. The nanotubes consisted of bonded nanoparticles with an average size of around 20 nm. Many nanopores were observed within the spaces between adjacent SnO_2 nanoparticles which could be due to the decomposition of PVP. The high resolution TEM (HRTEM) image in Fig 3a (iii) shows well resolved lattice fringes, signifying that the SnO_2 nanoparticle in the nanotube possessed excellent crystallinity. The lattice fringes with the d spacing of 0.264 nm corresponds to the (101) plane of tetragonal SnO_2. The ring-shaped selected area electron diffraction (SAED) pattern (inset of Fig. 3a (iii)) indicates that the SnO_2 nanofibers were polycrystalline, in good accordance with the XRD data described above.

Fig. 3b and 3c further illustrates the hierarchical TiO_2 nano-architecture arrays constituted by an assembly of multi-scale nanoflakes based on 7 and 24 hrs of growth duration. The TEM observations coincide well with the FESEM images shown earlier. These sequential images reveal a morphological and structural transformation from pristine SnO_2 nanofibers to TiO_2-SnO_2 hierarchical nanostructures. With SnO_2 nanofibers as the building block, the TiO_2 nanoflakes started to germinate and form the tiny branch-like nanostructures surrounding the entire nanofibers after 7 hrs of growth duration. With increased hydrothermal growth duration, higher surface coverage density was achieved and the structure of the nanoflakes becomes more prominent. Extending the hydrothermal growth duration to 24 hrs resulted in prominent TiO_2 nanoflakes that were compactly developed on the surfaces of SnO_2 nanofibers. The length of the nanoflakes could reach up to around 50 nm (Fig. 3c (ii)). The clear lattice fringes of the TiO_2 nanoflakes were observed from the HRTEM images. The interplanar spacing obtained from the lattice fringes along d(110) was 0.325 nm, which could be assigned to the rutile TiO_2 (110). The lattice constant spacing with 0.250 nm pertained to the d-spacing of rutile TiO_2 (101) crystal planes. These results confirmed that the hierarchical heterostructures with TiO_2 nanoflakes on SnO_2 nanofibers were well created.

The successfully growth of TiO_2 nanoflakes onto the surface of SnO_2 nanofibers can be explained by the recrystallization process which involved the dissolve and grow method.[32,33] During the hydrothermal growth process, The Ti species from TTIP precursor reacts with concentrated acidic solution to form $TiCl_3$. The Ti^{3+} species formed are not stable. Hence, it will immediately react with water to form $TiOH^{2+}$. Finally, the $TiOH^{2+}$ is oxidized into Ti(IV) from the reaction with dissolved oxygen. These Ti(IV) complex ions act as the growth units to form nanostructures. The overall growth process can be described as follow:

$$2Ti + 6HCl \rightarrow 2TiCl_3 + H_2O \quad (1)$$

$$Ti^{3+} + H_2O \rightarrow TiOH^{2+} + H^+ \quad (2)$$

$$TiOH^{2+} + O_2 \rightarrow Ti(IV)\text{-}oxo\ species + O_2^- \rightarrow TiO_2 \quad (3)$$

RSC Advances

ARTICLE

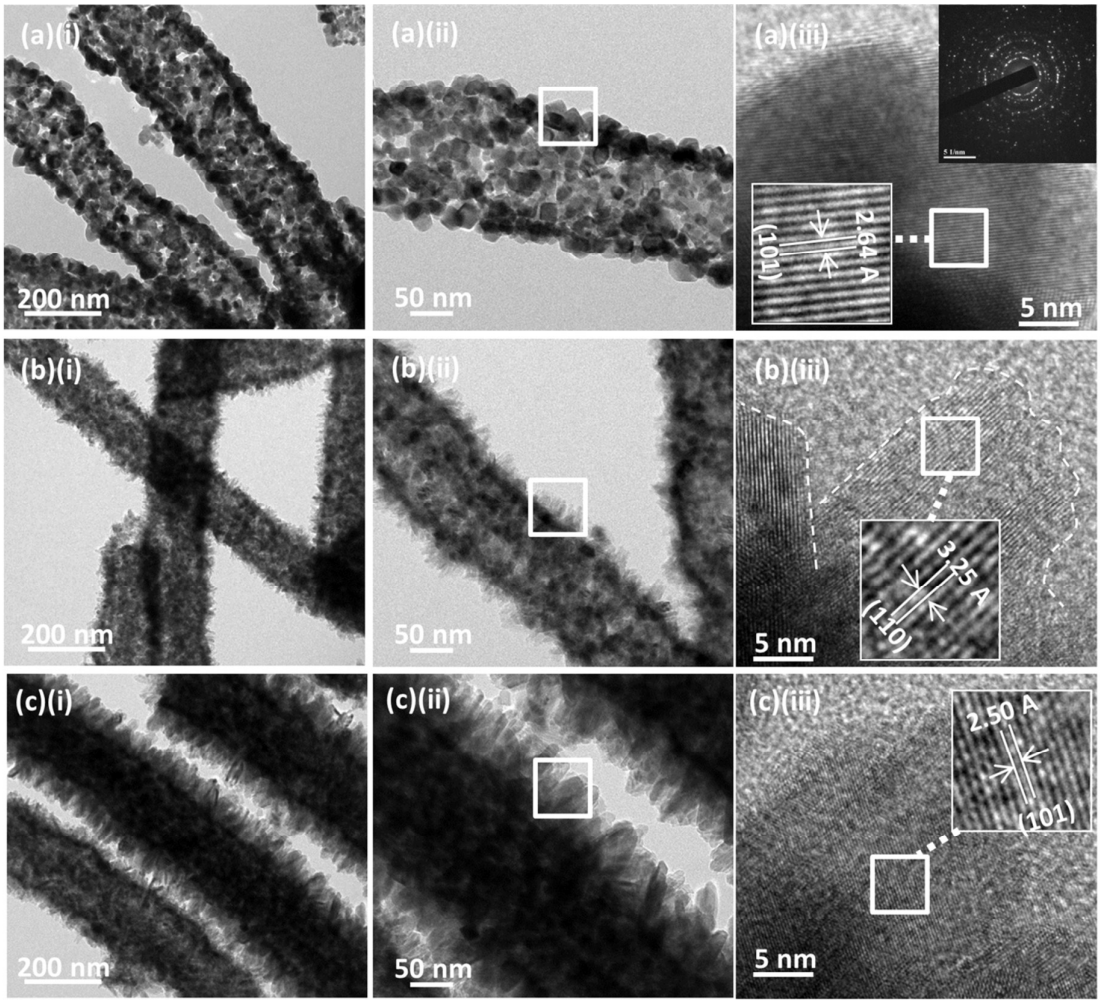

Figure 3. (a) TEM and HRTEM images of SnO_2 nanofibers. The inset in (a-iii) is the SAED patterns reveal the crystallinity of SnO_2. Selected TiO_2-SnO_2 hierarchical heterostructures hydrothermally grown at different durations; (b) 7 hrs; (c) 24 hrs.

3.2 Photovoltaic performance

The hierarchical TiO_2-SnO_2 nanostructures were fabricated into the photoelectrode for DSSCs. A total of five DSSCs based on SnO_2 nanofibers and TiO_2-SnO_2 hierarchical nanostructures as photoelectrode were fabricated for study. Fig.4 depicts photovoltaic performance of DSSC with hydrothermal growth of TiO_2 nanoflakes/SnO_2 nanofibers. The corresponding photovoltaic parameters such as short-circuit current density (J_{SC}), open-circuit voltage (V_{OC}), fill factor (*FF*), and conversion efficiency (η) derived from the photocurrent density-voltage (*J-V*) curves were summarized in Table 1.

The DSSC with pristine SnO_2 nanofibers as photoelectrode (sample SS) showed very poor photovoltaic performance, with the overall power conversion efficiency of less than 1.0 %. As mentioned previously, this result can be attributed to the lower electron trapping density of SnO_2, which has been reported to be the key in retarding interfacial charge recombination dynamics in DSSC.[13] Consequently, the high interfacial charge recombination resulted in low V_{OC} by decreasing the concentration of electrons in the conduction band of the semiconductor. With reduced forward injection current, the J_{SC} value was also limited.[47,48]

By utilizing the TiO_2-SnO_2 hierarchical nanostructures as photoelectrode, the conversion efficiencies of the DSSCs improved drastically. The best cell (Sample TS24) delivered a conversion efficiency of 3.73 %, demonstrated more than 4-fold improvement over the DSSC with pristine SnO_2 nanofibers as photoelectrode. Noticeable increments in the photovoltaic parameters were also observed. The improvement in the V_{OC} value can be explained from the formation of this double-layered TiO_2-SnO_2 structure that creates a surface dipole layer that is dependent on the isoelectric point of the materials involved.[49,50] The isoelectric point of TiO_2 is higher than SnO_2 and hence it yields a surface dipole layer towards the SnO_2. This dipole layer might shift the conduction band of SnO_2 to a more negative value, causing an increase in V_{OC}. The prominent increases in J_{SC} and *FF* also indicate that the interfacial charge recombination on SnO_2 electrodes were effectively suppressed by applying the TiO_2 nanoflakes on the SnO_2 nanofibers. The dark current measurement as shown in Fig. 4(b) was also carried out to investigate effectiveness of TiO_2-SnO_2 system for achieving high efficiency DSSC. The dark current can be used to represent the charge recombination between the electrons in photoelectrode and I_3^- ions in electrolyte.[51] Owing to lower conduction band energy level for SnO_2 than TiO_2, the SnO_2 establishes an expressway between TiO_2 and FTO glass to promote the transport of the photogenerated electrons. At the same time, the TiO_2 also acts as a barrier to effectively reduce the recombination of photogenerated electrons in anode and I_3^- ions in. As such, the dark currents for the TS-based solar cells were generally lower than the sample SS, which in turn improved the overall photovoltaic performance.

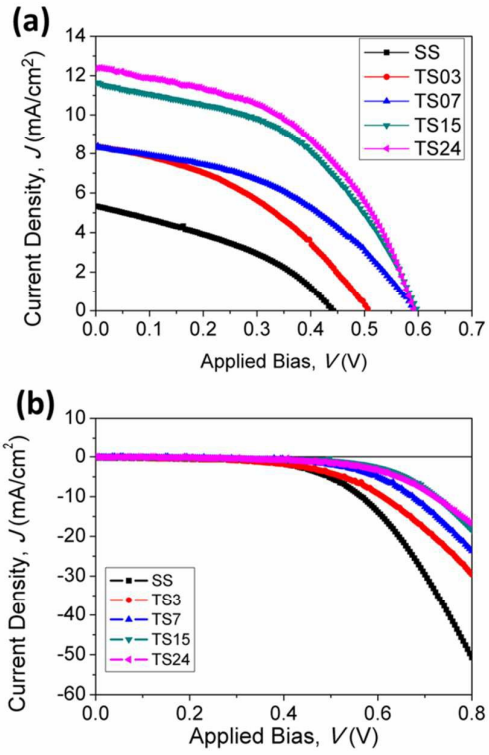

Figure 4. (a) Photovoltaic *J-V* curves for DSSCs with TiO_2-SnO_2 hierarchical heterostructures grown at different durations. (b) dark current measurements.

Table 1. Photocurrent density – Voltage *(J-V)* characteristic of DSSC with photoelectrode made from hierarchical TiO_2-SnO_2 nanostructures hydrothermally grown at different durations.

Samples	V_{OC} (V)	J_{SC} (mA/cm^2)	*FF* (%)	η (%)
SS	0.38	6.50	34.0	0.84
TS03	0.51	8.35	40.1	1.70
TS07	0.59	8.30	42.6	2.08
TS15	0.60	11.65	46.9	3.28
TS24	0.61	12.68	48.5	3.73

The sequential improvement of photovoltaic performance according to the growth duration of TiO_2 nanoflakes is explained as follows. In the first 3 and 7 hrs of growth, some back electron transfer from uncovered areas of SnO_2 nanofibers still existed. Hence, the improvement in the photovoltaic performances for sample TS03 and TS07 were relatively minor. When the hydrothermal growth duration was extended to 24 hrs, prominent TiO_2 nanoflakes formed densely on the surface of SnO_2 nanofiber to produce the hierarchical nano-architecture. This has greatly enhanced the coverage density to inhibit the back electron transfer and increased the surface area for dye loading. The dye-desorptions on these photoelectrodes were performed and the amount of dye absorbed onto the surface of TiO_2-SnO_2 hierarchical heterostructures (Sample TS24, 2.9 x 10^{-7} mol/cm^2) was found to be 61.1% greater than the pristine SnO_2 nanofibers (Sample SS, 1.8 x 10^{-7} mol/cm^2). (Supporting Information S5) The enhancement in the dye-loading as a result of increased specific surface area of the photoelectrode made from TiO_2-SnO_2 hierarchical nanostructures has directly contributed to higher J_{SC}.

In addition to higher dye loading capability, the hierarchical TiO_2-SnO_2 photoelectrode also appeared to possess enhanced light scattering ability. Enhanced light scattering ability of a photoelectrode is crucial for high light harvesting efficiency that contributes to higher photocurrent density of a DSSC.[52-54] The difference in the architecture of photoelectrode has a direct influence on the light scattering property of a DSSC.[55,56] As clearly perceived from the diffuse reflectance spectra of sample TS24 and SS in Fig. 5, the hierarchical TiO_2-SnO_2 film has higher diffuse reflection ability in the wavelength range from 430 nm to 800 nm. This suggests that the film possessed supreme light scattering capability, which allowed multiple light traveling paths to improve the light interactions with the dye-molecules anchored on the surface of the metal oxide. In contrast, the SnO_2 nanofiber film demonstrated comparatively poorer light scattering capability. This has resulted in the unabsorbed light to penetrate through the film with limited back-scattered light for multiple interactions. Hence, the light harvesting efficiency and photocurrent were relatively poor.

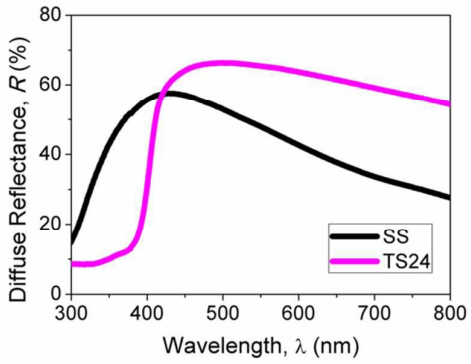

Figure 5. Comparison of diffuse reflectance spectra for SnO_2 nanofiber film and hierarchical TiO_2-SnO_2 nanocomposite film.

EIS has been widely employed to investigate the kinetics of electrochemical and photoelectrochemical system. It has been used to study the prominent electronic and ionic processes in DSSCs.[57,58] To distinguish the difference in the interfacial characteristics of these photoelectrodes, the EIS spectra of the DSSCs were measured at an applied bias of V_{OC} and a frequency range from 0.1 Hz to 100 kHz, with ac amplitude of 10 mV in a simulated solar light. Fig. 6 shows EIS spectra of the DSSCs with the photoelectrode made from SnO_2 nanofiber and hierarchical TiO_2-SnO_2, respectively. In general, 3 semicircles in the order of increasing frequency can be observed from the Nyquist plot. The low frequency region is attributed to the Nernst diffusion within the electrolyte, while the intermediate frequency features the electron transport in the oxide semiconductor/dye/electrolyte interface. Lastly, the high frequency peak corresponds to the charge transfer at the platinum coated counter electrode. The equivalent circuit diagrams were fitted based on the general transmission line model for DSSCs is shown in the inset of Fig. 6a.

Since the EIS measurements were carried out at open-circuit potential bias, there was no current passing through the external circuit. The photogenerated electrons injected from the dye molecules into the oxide semiconductor must be recombined by I_3- ions at this interface. Hence, the R_μ resistance shown in the Nyquist plot represents a net charge-transfer resistance at the oxide semiconductor/dye/electrolyte interface. With higher dye-loading for sample TS24, more photogenerated electrons were injected into the oxide semiconductor under illumination. Consequently, the net charge-transfer resistance at this interface was much lower for sample TS24 as compared to sample SS.

The lifetime of photogenerated electrons in the oxide film (t_r) can be estimated from the maximum angular frequency (ω_{max}) of the impedance semicircle arc at middle frequencies, according to the relation $t_r = 1/\omega_{max} = 1/2\pi f_{max}$, where f_{max} is the maximum frequency of the mid-frequency peak.[59] As shown in the inset of Fig.6b, the f_{max} value for sample TS24 is 7.14 Hz ($t_{r\text{-}TS24}$ = 22.3 ms), much lower than the values for sample SS at 10.99 Hz ($t_{r\text{-}SS}$ = 14.5ms). These data suggest that photogenerated electrons in the hierarchical TiO_2-SnO_2 film have a longer lifetime than in SnO_2 nanofiber film. This increment in the t_r value corresponds to the effective retardation of the charge recombination reaction between photoinjected electrons with I_3^- during the electron transport through the film made with hierarchical TiO_2-SnO_2 composite.

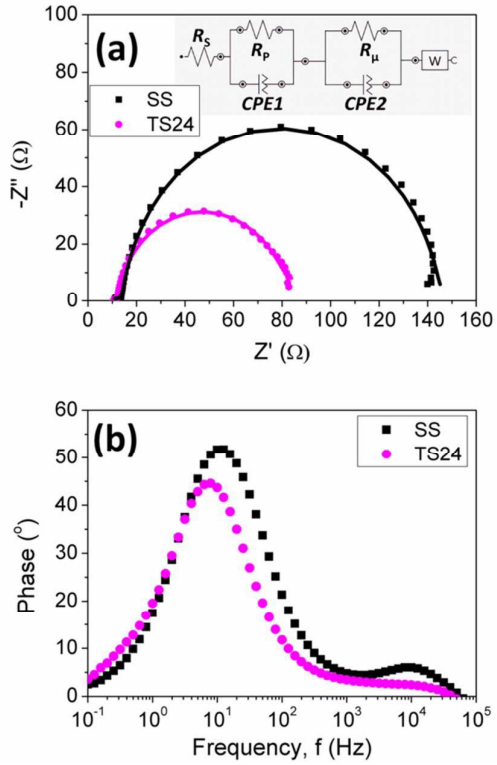

Figure 6. (a) Nyquist plot of DSSCs with SnO_2 nanofibers and hierarchical TiO_2-SnO_2 heterostructures as photoelectrode under simulated sunlight illumination. Inset shows the equivalent circuit diagram. (b) Corresponding Bode phase plot.

Although SnO_2 is always considered as a potential material for photoelectrode, the DSSC with SnO_2 photoelectrodes generally shows lower conversion efficiency as compared to its TiO_2 counterpart due to its inherently larger charge recombination, slower charge injection and poorer dye-loading. This study has demonstrated that proper design of SnO_2 photoelectrodes can be used to alleviate these issues. The hierarchical nanostructure of TiO_2-SnO_2 employed for DSSC has led to improved photovoltaic performance with respect to those based on pristine SnO_2 nanofiber. The proposed architecture is efficient for DSSC with SnO_2 photoelectrode due to the larger surface area for dye-loading, inhibition of back-electron transfer, better carrier lifetime and enhanced light scattering effects.

However, the improved conversion efficiency is still inferior with reference to the state of the art DSSC. The overall low conversion efficiency might be attributed to lower dye-loading in these photoelectrodes deposited in this work, in contrast to a typical DSSC with densely packed nanoparticles film. The thicknesses of the SnO_2 layer used in this study were controlled to be around ~ 6 um for better consistency. It is believed that increasing the thickness of SnO_2 layer can

improve the overall dye-loading to further enhance the short circuit current density. Besides that, large pores between the nanofibers could be observed from the SEM images. This has caused a less compact structure and affected the dye-loading and thus the overall efficiency.

4. Conclusions

In summary, the hierarchical hybrid architecture with TiO_2 nanoflakes on SnO_2 nanofibers has been successfully developed by combining the electrospinning and single-step hydrothermal growth method. The high-surface to volume ratio of this hierarchical hybrid nanostructure, along with the appropriate combination of materials, makes it an excellent candidate for photoelectrode in DSSC. In general, the DSSC made using hierarchical hybrid nanostructure of TiO_2-SnO_2 demonstrated improved photovoltaic performance compared to those based on pristine SnO_2 nanofiber. As the hydrothermal growth duration increases, the makeover of tubular structure of SnO_2 nanofiber to hierarchical hybrid architecture of TiO_2-SnO_2 was successfully achieved, leading to higher specific surface area. The back electron transfer for recombination in this hierarchical hybrid structure has been successfully retarded. Consequently, the lifetime of the photogenerated electron transported through the hierarchical matrix was improved. The synergistic effects from all these factors, together with the excellent light scattering ability has contributed to extraordinary improvement of photocurrent density, open circuit potential and the fill factor of the DSSC. These improvements have in turn transformed into a remarkable 4-fold improvement in the photovoltaic power conversion efficiency of the DSSC made from the well-defined TiO_2 nanoflakes on SnO_2 nanofibers hydrothermally grown for 24 hrs. This work suggests that this novel hierarchical nanostructure synthesized through this facile method may serve as a new generation photoelectrode for high efficiency DSSC. On top of that, its potential applications are foreseeable to be extended and implemented in other fields such as photocatalysis and charge storage.

References

1 B. O'Regan and M. Grätzel, Nature, 1991, 353, 737-740.
2 M. K. Nazeeruddin, S. M. Zakeeruddin, R. Humphry-Baker, M. Jirousek, P. Liska, N. Vlachopoulos, V. Shklover, C.-H. Fischer and M. Grätzel, Inorganic Chemistry, 1999, 38, 6298-6305.
3 C.-Y. Chen, M. Wang, J.-Y. Li, N. Pootrakulchote, L. Alibabaei, C.-h. Ngoc-le, J.-D. Decoppet, J.-H. Tsai, C. Grätzel, C.-G. Wu, S. M. Zakeeruddin and M. Grätzel, ACS Nano, 2009, 3, 3103-3109.
4 S. Mathew, A. Yella, P. Gao, R. Humphry-Baker, F. E. CurchodBasile, N. Ashari-Astani, I. Tavernelli, U. Rothlisberger, K. NazeeruddinMd and M. Grätzel, Nat Chem, 2014, 6, 242-247.
5 M. Liu, M. B. Johnston and H. J. Snaith, Nature, 2013, 501, 395-398.
6 G. Calogero, A. Bartolotta, G. Di Marco, A. Di Carlo and F. Bonaccorso, Chemical Society Reviews, 2015, 44, 3244-3294.
7 G. Calogero, J. H. Yum, A. Sinopoli, G. Di Marco, M. Grätzel and M. K. Nazeeruddin, *Solar Energy*, 2012, 86, 1563-1575.
8 C. Sandquist and J. L. McHale, Journal of Photochemistry and Photobiology A: Chemistry, 2011, 221, 90-97.
9 L. Y. Chang, C. P. Lee, C. T. Li, M. H. Yeh, K. C. Ho and J. J. Lin, Journal of Materials Chemistry A, 2014, 2, 20814-20822.
10 J. Burschka, A. Dualeh, F. Kessler, E. Baranoff, N. L. Cevey-Ha, C. Yi, M. K. Nazeeruddin and M. Grätzel, Journal of the American Chemical Society, 2011, 133, 18042-18045.
11 I. Chung, B. Lee, J. He, R. P. H. Chang and M. G. Kanatzidis, Nature, 2012, 485, 486-489.
12 M. J. Ju, I. Y. Jeon, J. C. Kim, K. Lim, H. J. Choi, S. M. Jung, I. T. Choi, Y. K. Eom, Y. J. Kwon, J. Ko, J. J. Lee, H. K. Kim and J. B. Baek, Advanced Materials, 2014, 26, 3055-3062.
13 G. Calogero, F. Bonaccorso, O. M. Marago, P. G. Gucciardi and G. Di Marco, Dalton Transactions, 2010, 39, 2903-2909.
14 J. Liu, T. Luo, S. Mouli T, F. Meng, B. Sun and M. Li, Chemical Communications, 2010, 46, 472-474.
15 H. Sun, J. Deng, L. Qiu, X. Fang and H. Peng, Energy & Environmental Science, 2015, 8, 1139-1159.
16 S. Zhu, L. Shan, X. Chen, L. He, J. Chen, M. Jiang, X. Xie and Z. Zhou, RSC Advances, 2013, 3, 2910-2916.
17 L.-Y. Chen and Y.-T. Yin, Nanoscale, 2013, 5, 1777-1780.
18 H. J. Snaith and C. Ducati, Nano Letters, 2010, 10, 1259-1265.
19 A. Birkel, Y. G. Lee, D. Koll, X. V. Meerbeek, S. Frank, M. J. Choi, Y. S. Kang, K. Char and W. Tremel, Energy and Environmental Science, 2012, 5, 5392-5400.
20 S. Yang, H. Kou, J. Wang, H. Xue and H. Han, Journal of Physical Chemistry C, 2010, 114, 4245-4249.
21 X. Jin, C. Liu, J. Xu, Q. Wang and D. Chen, RSC Advances, 2014, 4, 35546-35553.
22 S. S. Shin, J. S. Kim, J. H. Suk, K. D. Lee, D. W. Kim, J. H. Park, I. S. Cho, K. S. Hong and J. Y. Kim, ACS Nano, 2013, 7, 1027-1035.
23 S. Gubbala, V. Chakrapani, V. Kumar and M. K. Sunkara, Advanced Functional Materials, 2008, 18, 2411-2418.
24 N. G. Park, M. G. Kang, K. S. Ryu, K. M. Kim and S. H. Chang, Journal of Photochemistry and Photobiology A: Chemistry, 2004, 161, 105-110.
25 A. N. M. Green, E. Palomares, S. A. Haque, J. M. Kroon and J. R. Durrant, Journal of Physical Chemistry B, 2005, 109, 12525-12533.
26 A. Kay and M. Grätzel, Chemistry of Materials, 2002, 14, 2930-2935.
27 J. B. Asbury, E. Hao, Y. Wang, H. N. Ghosh and T. Lian, Journal of Physical Chemistry B, 2001, 105, 4545-4557.
28 S. Anderson, E. C. Constable, M. P. Dare-Edwards, J. B. Goodenough, A. Hamnett, K. R. Seddon and R. D. Wright, Nature, 1979, 280, 571-573.
29 S. Ardo and G. J. Meyer, Chemical Society Reviews, 2009, 38, 115-164.
30 S. H. Ahn, D. J. Kim, W. S. Chi and J. H. Kim, Advanced Materials, 2013, 25, 4893-4897.
31 C. Gao, X. Li, B. Lu, L. Chen, Y. Wang, F. Teng, J. Wang, Z. Zhang, X. Pan and E. Xie, Nanoscale, 2012, 4, 3475-3481.
32 J. Huo, Y. Hu, H. Jiang, W. Huang and C. Li, Journal of Materials Chemistry A, 2014, 2, 8266-8272.
33 P. Docampo, P. Tiwana, N. Sakai, H. Miura, L. Herz, T. Murakami and H. J. Snaith, Journal of Physical Chemistry C, 2012, 116, 22840-22846.
34 M. K. I. Senevirathna, P. K. D. D. P. Pitigala, E. V. A. Premalal, K. Tennakone, G. R. A. Kumara and A. Konno, Solar Energy Materials and Solar Cells, 2007, 91, 544-547.
35 C. Prasittichai and J. T. Hupp, Journal of Physical Chemistry Letters, 2010, 1, 1611-1615.
36 K. Zhu, N. R. Neale, A. Miedaner and A. J. Frank, Nano Letters, 2007, 7, 69-74.

37 Z. Sun, J. H. Kim, Y. Zhao, D. Attard and S. X. Dou, Chemical Communications, 2013, 49, 966-968.
38 S. S. Mali, H. Kim, W. Y. Jang, H. S. Park, P. S. Patil and C. K. Hong, ACS Sustainable Chemistry and Engineering, 2013, 1, 1207-1213.
39 T. Krishnamoorthy, V. Thavasi, M. Subodh G and S. Ramakrishna, Energy & Environmental Science, 2011, 4, 2807-2812.
40 S. Cavaliere, S. Subianto, I. Savych, D. J. Jones and J. Rozière, Energy and Environmental Science, 2011, 4, 4761-4785.
41 E. N. Kumar, R. Jose, P. S. Archana, C. Vijila, M. M. Yusoff and S. Ramakrishna, Energy and Environmental Science, 2012, 5, 5401-5407.
42 Z. Liu, D. D. Sun, P. Guo and J. O. Leckie, Nano Letters, 2007, 7, 1081-1085.
43 X. Peng, A. C. Santulli, E. Sutter and S. S. Wong, Chemical Science, 2012, 3, 1262-1272.
44 S. Jiang, B. Zhao, R. Ran, R. Cai, M. O. Tade and Z. Shao, RSC Advances, 2014, 4, 9367-9371.
45 L. Wang, X. Luo, X. Zheng, R. Wang and T. Zhang, RSC Advances, 2013, 3, 9723-9728.
46 L. Xu, R. Xing, J. Song, W. Xu and H. Song, Journal of Materials Chemistry C, 2013, 1, 2174-2182.
47 D. Cahen, G. Hodes, M. Grätzel, J. F. Guillemoles and I. Riess, Journal of Physical Chemistry B, 2000, 104, 2053-2059.
48 M. K. Nazeeruddin, A. Kay, I. Rodicio, R. Humphry-Baker, E. Müller, P. Liska, N. Vlachopoulos and M. Grätzel, Journal of the American Chemical Society, 1993, 115, 6382-6390.
49 Y. Diamant, S. Chappel, S. G. Chen, O. Melamed and A. Zaban, Coordination Chemistry Reviews, 2004, 248, 1271-1276.
50 Q. Zhang and G. Cao, Nano Today, 2011, 6, 91-109.
51 S. Ito, P. Liska, P. Comte, R. Charvet, P. Pechy, U. Bach, L. Schmidt-Mende, S. M. Zakeeruddin, A. Kay, M. K. Nazeeruddin and M. Grätzel, Chemical Communications, 2005, DOI: 10.1039/b505718c, 4351-4353.
52 G. Shang, J. Wu, S. Tang, M. Huang, Z. Lan, Y. Li, J. Zhao and X. Zhang, Journal of Materials Chemistry, 2012, 22, 25335-25339.
53 E. Ramasamy and J. Lee, Journal of Physical Chemistry C, 2010, 114, 22032-22037.
54 Q. Zhang, D. Myers, J. Lan, S. A. Jenekhe and G. Cao, Physical Chemistry Chemical Physics, 2012, 14, 14982-14998.
55 Y. F. Wang, J. W. Li, Y. F. Hou, X. N. Yu, C. Y. Su and D. B. Kuang, Chemistry - A European Journal, 2010, 16, 8620-8625.
56 J. Qian, P. Liu, Y. Xiao, Y. Jiang, Y. Cao, X. Ai and H. Yang, Advanced Materials, 2009, 21, 3663-3667+3617.
57 Q. Wang, J. E. Moser and M. Grätzel, Journal of Physical Chemistry B, 2005, 109, 14945-14953.
58 F. Fabregat-Santiago, J. Bisquert, G. Garcia-Belmonte, G. Boschloo and A. Hagfeldt, Solar Energy Materials and Solar Cells, 2005, 87, 117-131.
59 R. Kern, R. Sastrawan, J. Ferber, R. Stangl and J. Luther, Electrochimica Acta, 2002, 47, 4213-4225.

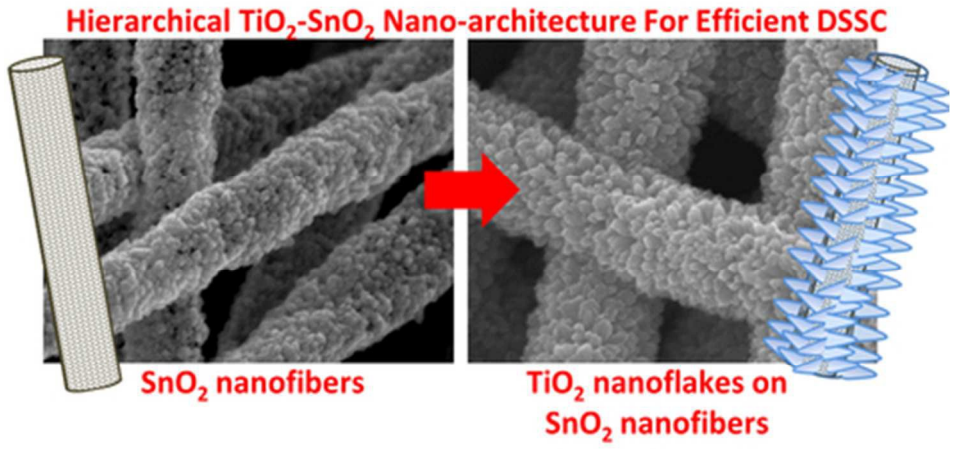

39x19mm (300 x 300 DPI)